Research Letter

How to cite: *J. Inorg. Mater.*, XXXX, XX(XX): XXXX
DOI:10.15541/jim20260026

Fabrication of ZrB_2/(SiC-AlN) Ceramic Composites *via* SiC and ZrB_2 precursors

ZHOU Yan[1,2], LIU Qikai[2], XIA Aidong[2,3], ZHANG Buhao[2,4], YIN Jie[2,3], HUANG Zhengren[2,3]

(1. School of Materials Science and Engineering, Shanghai University, Shanghai 200444, China; 2. Shanghai Institute of Ceramics, Chinese Academy of Sciences, Shanghai 201899, China; 3. College of Materials Science and Opto-Electronic Technology, University of Chinese Academy of Sciences, Beijing 100864, China; 4. Faculty of Engineering, University of Nottingham, Nottingham NG7 2RD, UK)

Abstract: In response to the demanding requirements of extreme high-temperature structural applications, such as thermal protection systems for hypersonic vehicles, ZrB_2/(SiC-AlN) ceramic composites were fabricated *via* a precursor-derived route using commercially available polycarbosilane and polyborozirconoxane, followed by hot-press sintering at 1950 ℃. X-ray diffraction results indicated the formation of hexagonal SiC and ZrB_2 phases after sintering, while no distinct AlN diffraction peaks were observed due to the formation of a SiC-AlN solid solution. Microstructural observations revealed that *in situ* formed ZrB_2 was uniformly dispersed within the SiC-AlN matrix, contributing to improved densification and inhibition of grain growth. The effects of precursor-derived ZrB_2 content on phase composition, microstructure, densification behavior, and mechanical properties of the composites were systematically investigated. Among the series of samples, the composite containing 25% ZrB_2 and 10% AlN (in mass) exhibited the lowest open porosity (0.6%), the highest flexural strength ((407±14) MPa), and the maximum fracture toughness ((5.8±0.1) MPa·$m^{1/2}$). This composition also exhibited effective short-term oxidation resistance in static air over the temperature range of 800–1000 ℃. The results demonstrate that the precursor-derived introduction of ZrB_2 is an effective approach to tailor microstructure and enhance the overall performance of polymer-derived SiC-AlN ceramic composites.

Keywords: precursor-derived ceramic; nanocomposite; SiC-AlN solid solution; toughness; strength

Silicon carbide (SiC) ceramics are widely recognized for their exceptional thermal and mechanical properties, including a thermal conductivity of 120–150 W/(m·K), a low coefficient of thermal expansion ((4–5)×10^{-6} $℃^{-1}$), compressive strength exceeding 2 GPa, flexural strength ranging from 350 to 500 MPa, and fracture toughness between 3.5 and 5.0 MPa·$m^{1/2}$[1-3]. Owing to these properties and their superior resistance to high temperatures, corrosion, and wear, SiC ceramics have become key materials in aerospace propulsion systems, nuclear reactors, and ultrahigh-temperature industrial equipment[4]. However, their mechanical performance is limited by incomplete densification and grain coarsening resulting from conventional sintering. To overcome these drawbacks, innovative compositional strategies have been proposed, including the incorporation of secondary phases to enhance mechanical properties[5]. The addition of AlN has been shown to promote heterogeneous grain growth, leading to improved densification. Su *et al.*[6] achieved a relative density of 99.1% in SiC ceramics with *in situ* synthesized AlN. ZrB_2 has also been utilized to enhance densification and mechanical properties. Chen *et al.*[7] reported that the mass addition of 20% ZrB_2 to SiC ceramics elevated flexural strength to 330 MPa. Despite these advancements, high-temperature sintering techniques often introduce

Received date: 2026-01-16; **Revised date:** 2026-03-04

Foundation item: National Natural Science Foundation of China (U22A20129, U23A2056); National Key R&D Program of China (2022YFB3706300)

Biography: ZHOU Yan (2002–), male, Master candidate. E-mail: zyan@hnu.edu.cn
周岩(2002–), 男, 硕士研究生. E-mail: zyan@hnu.edu.cn

Corresponding author: ZHANG Buhao, PhD. E-mail: buhaozhang@hotmail.com; YIN Jie, professor. E-mail: jieyin@mail.sic.ac.cn
张步豪, 博士. E-mail: buhaozhang@hotmail.com; 殷杰, 研究员. E-mail: jieyin@mail.sic.ac.cn

tradeoffs between scalability and microstructural uniformity[8].

Polymer-derived ceramics (PDCs) offer a breakthrough by enabling the fabrication of SiC ceramics with nanoscale grains, which improve densification and enhance thermal and mechanical properties[9-10]. Thus, PDC-based SiC ceramics have become a transformative solution for next-generation applications, including fusion energy systems, high-speed aerospace components, and advanced heat exchangers[11]. In principle, the PDC route can mitigate grain coarsening and enable the formation of dense microstructures suitable for harsh environments. Yu *et al*.[12] achieved near-theoretical densification (99%) of PDC-SiC/Si_3N_4 *via* hot isostatic pressing. However, the resulting ceramics exhibited limited fracture toughness (4.8 MPa·$m^{1/2}$). Pressureless sintering of PDC-SiC ceramics, as explored by Chowdhury *et al*.[13] and Wang[14], resulted in densities of 95% and 98%, respectively, with low thermal conductivities (20–25 W/(m·K)). Advanced methods, such as spark plasma sintering (SPS) demonstrated by Bechelany *et al*.[15], achieved near-complete densification (~100%) and high hardness (15 GPa). However, scalability for large or complex geometries remains a significant limitation. While Santhosh *et al*.[16] emphasized the importance of grain size control (30–70 nm) in achieving thermal conductivity (30 W/(m·K)) and flexural strength (550 MPa), their reaction bonding process posed challenges in sintering time and scalability. In contrast, alternative approaches, such as stereolithography explored by He *et al*.[17] and Liu *et al*.[18], yielded suboptimal densities (~83%), which severely compromised the resulting mechanical performance.

Addressing these challenges, Xia *et al*.[19] demonstrated the effectiveness of ZrB_2 as an additive in PDC-SiC ceramics. Using hot-pressing at 1950 ℃ under 40 MPa, they achieved a relative density of 95.4%, along with markedly improved flexural strength (579 MPa) and fracture toughness (6.7 MPa·$m^{1/2}$). These results underscore the potential of ZrB_2 to enhance both the densification and overall performance of SiC-based systems, thereby offering a promising strategy to overcome the limitations of current fabrication routes. However, the simultaneous use of SiC and ZrB_2 precursors to fabricate PDCs *via* precursor-derived routes remains unexplored.

The simultaneous optimization of these properties, particularly in heterogeneous systems, presents significant challenges[20-21]. Key gaps include achieving stable grain refinement, strong interfacial bonding, and balanced thermo-mechanical properties[22]. The PDC route offers a distinctive method for fabricating SiC-based ceramics through the controlled pyrolysis of preceramic polymers such as polycarbosilane (PCS), resulting in nanostructured ceramics with nanoscale grains and amorphous phases. However, pyrolysis-induced defects, such as pores and cracks caused by gas release, significantly compromise the densification and mechanical reliability[15, 23]. Therefore, advanced precursor designs, pyrolysis optimization, and densification strategies for PDC-SiC ceramics is essential to overcome these limitations[17, 24]. Co-doping PDC-SiC ceramics with AlN and nanosized ZrB_2 has been shown to enhance their mechanical properties[25]. However, achieving uniform dispersion and homogeneity in these nano/microhybrid powders remains a significant challenge[19].

In this study, ZrB_2/(SiC-AlN) ceramic composites were fabricated using a precursor-derived method with commercially available PCS and polyborozirconoxane. Compared to conventional powder-added routes, the precursor-derived introduction of ZrB_2 achieves superior densification and enhanced mechanical performance of PDC-based SiC-AlN composites. The relationships among ZrB_2 content, microstructural features, mechanical properties, and oxidation behavior were systematically investigated.

1 Experimental

1.1 Raw materials

Liquid PCS (purity ≥ 99.5%) was obtained from the Institute of Chemistry, Chinese Academy of Sciences (ICCAS), China, and used as the SiC precursor. Dicumyl peroxide (DCP, ICCAS, China) was employed as the cross-linking agent. Liquid polyborozirconoxane (purity 97%, ICCAS, China) was used as the ZrB_2 precursor. Commercial aluminum nitride powder (AlN, 100 nm, purity ≥ 99.5%) was obtained from Tokuyama Co., Japan.

1.2 Cross linking

First, 0.4% (in mass) DCP was added to liquid PCS. The mixture was dispersed for 10 min and then placed in a vacuum oven. Under a vacuum environment, the temperature was raised to 150 ℃ at a heating rate of 5 ℃/min for curing and held for 2 h. Similarly, the ZrB_2 precursor was cured by heating to 120 ℃ at the same rate and maintained for 1 h. Subsequently, both cross-linked precursors were ground separately into powders.

1.3 Preparation of nanocomposite ceramic

The cross-linked SiC and ZrB_2 precursor powders

were mixed with AlN (mass fraction of 10%, determined as the optimal content for achieving a synergistic effect within the ZrB_2/(SiC-AlN) system based on our previous systematic optimization[19]), ethanol, and SiC balls. The mixture was then ball-milled at 300 r/min for 4 h. The slurry was subsequently dried at 60 ℃ for 12 h, passed through a 100-mesh (149 μm) sieve, and heated at 1200 ℃ under an Ar atmosphere. The resulting pyrolyzed powder mixture was sieved again and placed in a 40 mm×40 mm graphite mold for hot pressing. Heating was conducted at a rate of 5 ℃/min up to 1950 ℃. External pressures of 20 and 40 MPa were applied upon reaching 1500 and 1750 ℃, respectively, and maintained until cooling. Samples with varying ZrB_2 mass fractions were prepared and labeled as P65A10Z25 (25% ZrB_2, in mass) and P45A10Z45 (45% ZrB_2, in mass). A comparison sample, designated P90A10, consisting of 90% PDC-SiC and 10% AlN (in mass) was also prepared to assess the effect of the ZrB_2 precursor.

1.4 Characterization

The open porosities of the sintered ZrB_2/(SiC-AlN) composites were measured using the Archimedes method. The specimens were ground and polished to a 0.5 μm finish using diamond abrasives. Flexural strength and elastic modulus were determined *via* three-point bending tests (Instron-1195, Instron, USA) with sample dimensions of 3 mm×4 mm×36 mm, following the GB/T 6569-2006 and GB/T 10700-2006 standards (China). The span was 30 mm and the crosshead rate was 0.5 mm/min. The fracture toughness (K_{IC}) was evaluated using a single-edge notched beam (SENB) test at a crosshead rate of 0.05 mm/min. Test strips were machined to 2.5 mm×5 mm×36 mm, with a 2.5 mm deep groove centered on the 2.5 mm×36 mm surface. A minimum of five specimens were tested to determine their average mechanical properties. X-ray diffractometer (XRD, Cu Kα radiation, D8 Advance, Bruker, Germany) was used to analyze phase composition and crystal structure of both the precursor and sintered samples. The 2θ angular was in the range of 10°–80°, with a step size of 0.02° and a dwell time of 0.3 s for all measurements. Scanning electron microscope (SEM, Thermo Scientific, Verios G4 UC, USA) and energy dispersive spectrometer (EDS, Ametek, USA) were used to examine the microscopic morphologies and elemental distributions of the samples.

2 Results and discussion

2.1 Precursor derived powders

The thermal decomposition of the ZrB_2 precursor was analyzed to establish its suitability for the fabrication of nanocomposite ceramics. The thermogravimetric analysis(TGA) curve shows a significant weight loss below 400 ℃, primarily due to solvent evaporation and initial precursor decomposition, which is corroborated by the corresponding endothermic peak in the differential scanning calorimetry(DSC) curve. The subsequent exothermic peak indicates further decomposition and precipitation of solid intermediates. The weight stabilized above 600 ℃, with a final ceramic yield of approximately 25% at 1400 ℃, confirming the formation of refractory phases(Fig. S1).

The phase evolution was determined by XRD analysis of the samples pyrolyzed at different temperatures (Fig. 1). At 1100 ℃, the product consisted mainly of monoclinic ZrO_2 (m-ZrO_2) with a minor amount of tetragonal ZrO_2 (t-ZrO_2). Upon increasing the temperature to 1300 ℃, the m-ZrO_2 phase diminished, t-ZrO_2 became more prominent, and diffraction peaks corresponding to crystalline ZrB_2 emerged. At 1500 ℃, the oxide phase was fully converted into ZrB_2. The progressive disappearance of ZrO_2 peaks suggests complete reduction through carbothermal reactions, as described by the following mechanism:

$$ZrO_2+B_2O_3+5C=ZrB_2+5CO \quad (1)$$

This reaction, thermodynamically favorable above 1230 ℃, progresses rapidly at higher temperatures and reaches completion at 1500 ℃[26].

Based on these results, 1500 ℃ was selected as the optimal pyrolysis temperature, ensuring complete conversion to the target ZrB_2 phase with efficient energy utilization, thereby providing a foundation for the synthesis of homogeneous ZrB_2/(SiC-AlN) nanocomposites.

Fig. 1 XRD patterns of the samples pyrolyzed at different temperatures

2.2 Phase analysis

The pyrolysis of SiC and ZrB_2 precursors (PCS, and polyborozirconoxane) at 1950 ℃ resulted in the formation of hexagonal SiC and ZrB_2 phases. In a previous study[24], we investigated the pyrolysis schedule of a PCS precursor. A series of ceramic composites were hot pressed at 1950 ℃ following the fabrication route described above. According to the phase diagram of SiC-AlN system[27], a solid solution of SiC and AlN is formed during sintering, which is consistent with the mutual migration and merging of their characteristic XRD bands. The hexagonal SiC phase was predominant in all samples (P90A10, P65A10Z25, and P45A10Z45). As shown in Fig. 2, P90A10 crystallized into 2H-SiC (PDF#29-1130), 4H-SiC (PDF#29-1127) and 3C-SiC (PDF#29-1129) at 1950 ℃. For the ZrB_2 precursor-doped samples P65A10Z25 and P45A10Z45, the relative intensities of the characteristic peaks corresponding to ZrB_2 phase (PDF#65-3389) became greater. A shift of 2H-SiC XRD peak toward a slightly higher angle was observed, which was likely attributable to residual strain at SiC/ZrB_2 interfaces. This strain may have developed during densification due to mismatch in thermal expansion coefficients or lattice parameters between the two phases, inducing interfacial stress and consequently leading to the observed peak shift. Moreover, a small amount of residual carbon originating from the pyrolysis of both the SiC and ZrB_2 precursors was detected at approximately 2θ=26.5°. This carbon is regarded as a chemically inert excess that primarily acts as a physical filler, which is consistent with the absence of new crystalline phases in the XRD patterns.

Fig. 2 XRD patterns of hot-pressed ZrB_2/(SiC-AlN) ceramic composites (P90A10, P65A10Z25, and P45A10Z45) at 1950 ℃

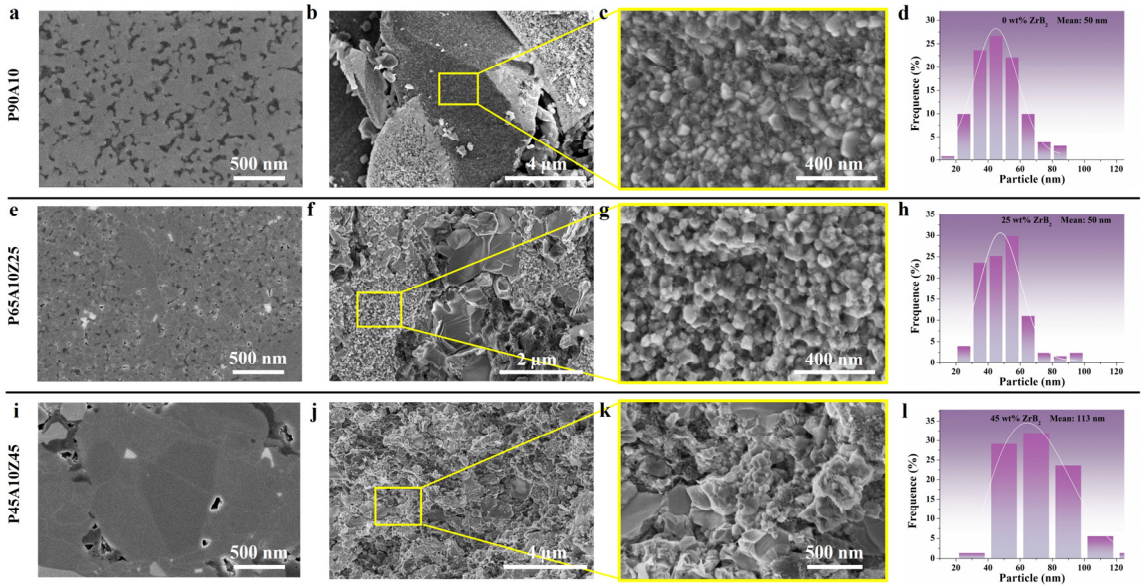

Fig. 3 (a, e, i) Polished surfaces, (b, c, f, g, j, k) fractured surfaces and (d, h, l) SiC grain size distribution of Hot-pressed ZrB_2/(SiC-AlN) ceramics

2.3 Microstructure evolution

The microstructural features of series of hot-pressed

ZrB_2/(SiC-AlN) samples are shown in Fig. 3. Based on the polished surface morphologies shown in Fig. 3(a, e, i), the grey particles correspond to SiC phase, the white particles to ZrB_2 phase, and the black areas represent residual carbon. This observation aligns with our previous study[19], which reported similar microstructural characteristics. Specifically, the precursor-derived ceramics exhibited large SiC clusters on the micron scale along with a dispersed distribution of ZrB_2 particles. All samples exhibited a small fraction of pores after hot pressing at 1950 ℃, with open porosity values below 2.9% (Table 1). Notably, P65A10Z25 exhibited the lowest open porosity (0.6%). Additionally, microcracks are formed owing to gas release during the pyrolysis of polycarbosilane. These microcracks are also observed in fracture surfaces, as shown in Fig. 3(b, f, j). Consistent with the polished surface analysis, micron-sized SiC clusters were more pronounced in fracture surface morphology, and nanoscale SiC particles were clearly visible in higher-magnification images (Fig. 3(c, g, k)).

According to Fig. 3(d, h), the average SiC grain size was 50 nm for both P90A10 and P65A10Z25, indicating a unimodal peak distribution. In contrast, the grain size of P45A10Z45 exhibited a bimodal distribution with an average size of 113 nm. The bimodal distribution in P45A10Z45 was likely a consequence of its high ZrB_2 precursor content, which can introduce local heterogeneities during pyrolysis and lead to differential grain growth during sintering. The relatively low temperature used during hot pressing inhibited the growth of SiC grains.

Table 1 Properties of the precursor-derived ZrB_2/(SiC-AlN) composites

Label	Open porosity/%	Flexural strength/MPa	Fracture toughness/(MPa·m$^{1/2}$)
P90A10	2.9	368±8	4.5±0.1
P65A10Z25	0.6	407±14	5.8±0.1
P45A10Z45	1.1	328±5	3.7±0.3

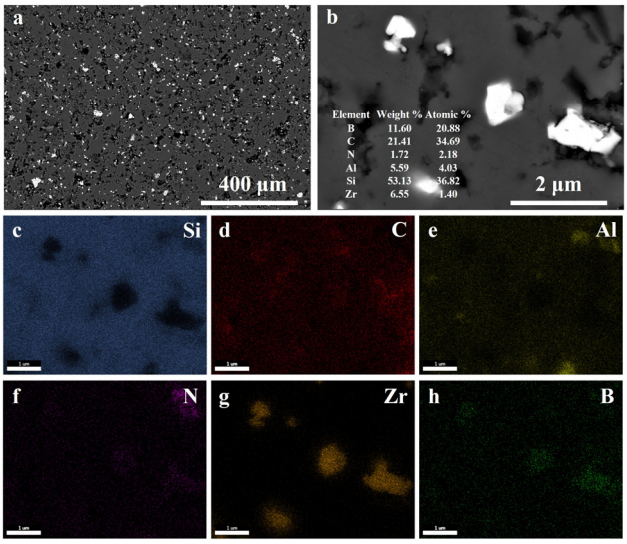

Fig. 4 (a, b) SEM images and (c-h) elemental mappings of the polished surface of P65A10Z25

The elemental distribution from EDS mappings provides definitive chemical evidence supporting the microstructural analysis, as shown in Fig. 4. The uniform signals of Zr and B correlated directly with the dispersed ZrB_2 particles, as observed by SEM. More importantly, Si, C, Al, and N exhibited highly overlapping and homogeneous distribution patterns across the mapped area. This provides strong evidence that SiC and AlN form a continuous solid-solution matrix rather than discrete phases. This conclusion was further corroborated by additional fracture surface analysis of the PCS-derived SiC fine-grain clusters (Fig. 5). The EDS elemental mappings of the representative fracture surface (Fig. 5(b−f)) demonstrated a uniform and coincident distribution of Si, C, Al, and N at submicron scale within matrix regions.

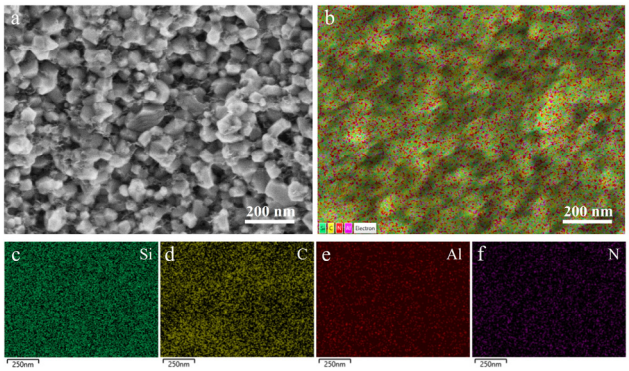

Fig. 5 (a) Morphology and (b-f) elemental mappings of the fracture surface of SiC-AlN solid-solution

2.4 Mechanical properties

Mechanical properties of all samples are listed in Table 1. Among them, the P65A10Z25 sample exhibited the most superior combination of properties, demon-

strating the lowest open porosity (0.6%), highest flexural strength ((407±14) MPa), and highest fracture toughness ((5.8±0.1) MPa·m$^{1/2}$). The exceptional performance of P65A10Z25 originated from the synergistic optimization of its microstructure. The role of *in situ*-formed ZrB_2 evolves with its content. At the optimal mass concentration (25%), it contributes synergistically: firstly as a densification facilitator, evidenced by the achievement of minimal open porosity (0.6%) which strengthens the matrix; secondly as a load-bearing reinforcing phase, where its uniform dispersion (Fig. 4) enables crack deflection and effective load transfer. This dual role is optimized for P65A10Z25. This synergy involves fine-grain strengthening from the *in situ* formed fine-grained SiC clusters and toughening mechanisms, such as crack deflection, induced by the uniformly dispersed *in situ* ZrB_2 particles.

A fine-grained structure was achieved, as the PCS-derived *in situ* SiC grains remained relatively small. During the rapid densification process of hot pressing, the inherent fineness of the starting phase effectively inhibited excessive grain growth in the matrix, contributing to the final ultrafine-grained microstructure in P65A10Z25.

Microstructural evolution was further evaluated in terms of the enhancement of macroscopic strength using classical strengthening models. To rationalize the observed strength trend, Hall-Petch relationship was employed for semi-quantitative assessment. The contribution of fine-grain strengthening is described by the Hall-Petch formula[28]:

$$\sigma_y = \sigma_a + kd^{-1/2} \quad (2)$$

where σ_y is yield strength, σ_a is friction stress, k is strengthening coefficient, and d is average grain diameter. The SiC grain size in P65A10Z25 (d_1≈50 nm) is significantly smaller than that in P45A10Z45 (d_2≈113 nm). The calculated $d_1^{-1/2}$ value is approximately 1.5 times that of $d_2^{-1/2}$, which is consistent with the measured flexural strength difference and provides trend-level support for the model. This calculation theoretically quantified the significant strength advantage of P65A10Z25 owing to grain refinement.

Similarly, an exponential porosity-strength relationship was used to highlight the importance of densification. The weakening effect of pores on strength (σ) follows an exponential decay relationship[29]:

$$\sigma = \sigma_b \cdot \exp(-bP) \quad (3)$$

where σ_b is the strength of theoretically dense material, b is a material constant, and P is open porosity. Compared to P90A10 sample (P_2=2.9%), the extremely low open porosity of P65A10Z25 (P_1=0.6%) accounts for a substantial increase in its strength retention ratio (σ_1/σ_2, where σ_1 and σ_2 are the flexural strengths of P65A10Z25 and P90A10, respectively), qualitatively indicating that densification was the dominant strengthening factor.

Furthermore, the *in situ* formed ZrB_2 particles are uniformly dispersed within the strengthened matrix (Fig. 4). This homogenized structure could prevent premature crack initiation caused by local enrichment of the second phase, while the strengthened matrix-particle interface ensured effective load transfer, enabling the composite to more fully utilize the load-bearing potential of each constituent phase.

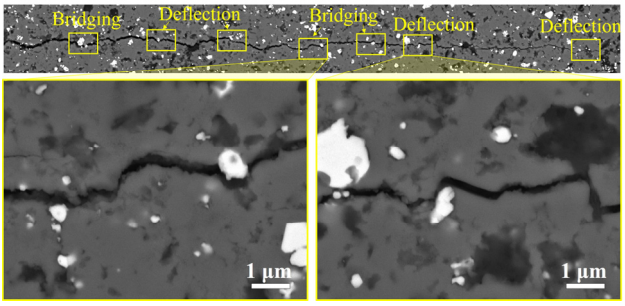

Fig. 6 Crack propagation path and characteristic features in P65A10Z25

In summary, the integration of a fine-grained SiC matrix, high densification, and uniform dispersion of *in situ* formed ZrB_2 particles collectively determine the optimal macroscopic mechanical properties through the synergistic action of Hall-Petch fine-grain strengthening, porosity-sensitive strength model, and effective load transfer from the reinforcement.

The peak fracture toughness ((5.8±0.1) MPa·m$^{1/2}$) exhibited by the P65A10Z25 sample is attributed to the synergistic activation of multiple toughening mechanisms induced by its optimized microstructure. The analysis of crack propagation path (Fig. 6) revealed a pronounced zigzag pattern, indicating significant crack deflection. This tortuous crack path was primarily driven by two key structural features: (i) crack pinning and deflection by the uniformly dispersed ZrB_2 particles acting as effective obstacles; (ii) crack bridging by the micron-sized SiC clusters and strong interfacial bonding, which generated crack-closure stresses. The concurrent operation of these mechanisms in P65A10Z25 led to substantial energy dissipation during fracture.

Notably, the lower fracture toughness of P45A10Z45 ((3.7±0.3) MPa·m$^{1/2}$), despite its higher nominal ZrB_2 content (45%, in mass), suggests the existence of a critical threshold for ZrB_2 addition. Exceeding this optimal

amount leads to microstructural degradation, which diminishes the toughening effectiveness.

This degradation was primarily due to two interconnected factors when ZrB_2 content surpassed the critical level. First, excessive precursor concentration promoted local agglomeration of ZrB_2 particles, rather than maintaining the uniform dispersion achieved in P65A10Z25. These agglomerates acted as stress concentrators. Concurrently, the increased gas released during pyrolysis of the excess precursor fostered the formation of microcracks (Fig. 4(j, k)). Both agglomerates and microcracks served as preferential sites for crack initiation and provided low-energy pathways for crack propagation, severely compromising the toughness.

Second, high fraction of the secondary phase (ZrB_2) disrupted the continuity of SiC-AlN solid-solution matrix. This is evidenced by the bimodal and larger grain size distribution (average 113 nm) observed in P45A10Z45 (Fig. 3(k)) compared to the finer, unimodal distribution (50 nm) in P65A10Z25. Relatively large grains were less effective in deflecting cracks. The compromised matrix also weakened interfacial bonding between ZrB_2 particles and matrix, reducing the effectiveness of both crack deflection and bridging mechanisms.

In conclusion, the results indicate that ZrB_2 addition is critical to fracture toughness. Superior toughness of P65A10Z25 was achieved at the optimal content, where a uniform microstructure enabled synergistic toughening. Beyond this threshold, as observed in P45A10Z45, the microstructural defects induced by excessive ZrB_2 override its intrinsic toughening benefits, leading to reduced performance.

2.5 Oxidation behavior

To further evaluate the high-temperature oxidation behavior and application potential of ZrB_2/(SiC-AlN) ceramic composites in static air, cyclic oxidation tests were conducted on all samples. The specimens were ground, polished, cleaned, dried, and placed in a muffle furnace under an air atmosphere. Oxidation was performed at 800, 1000, and 1200 ℃. The experiment at each temperature consisted of six consecutive holding cycles, each lasting 10 min, resulting in a cumulative oxidation time of 1 h, to simulate oxidation response under short-term thermal cycling conditions.

The oxidation products and mass loss behavior indicate that high-temperature oxidation leads to decomposition of ZrB_2 and volatilization of B_2O_3. As shown in the phase analysis in Fig. 7(a−c), diffraction peaks of Al_2O_3 and ZrO_2 were detected after oxidation, whereas no distinct peaks corresponding to SiO_2 or borate phases were observed. The absence of crystalline SiO_2 peaks (Fig. S2) is attributed to the formation of amorphous silica under the short-term oxidation conditions (800–1200 ℃, cyclic exposure for 1 h). In addition, although B_2O_3 may form during oxidation of ZrB_2, its relatively high vapor pressure at elevated temperatures promotes rapid volatilization, suppressing the stabilization of borosilicate phases. EDS analysis (Fig. S3) qualitatively supports this interpretation, showing oxygen and Zr enrichment in the oxide layer while no detectable boron remains on the surface[30]. The corresponding oxidation kinetics curves (mass loss *vs.* oxidation time) in Fig. 7(d−f) show that all samples exhibited net mass loss throughout the experiment at different temperatures. Moreover, the mass loss rate increased with increasing temperature. This behavior is primarily attributed to the continuous volatilization of B_2O_3, which forms *via* oxidation of the ZrB_2 component. Given its high vapor pressure at 800 ℃ and above, the volatilization of B_2O_3 dominates the net mass change.

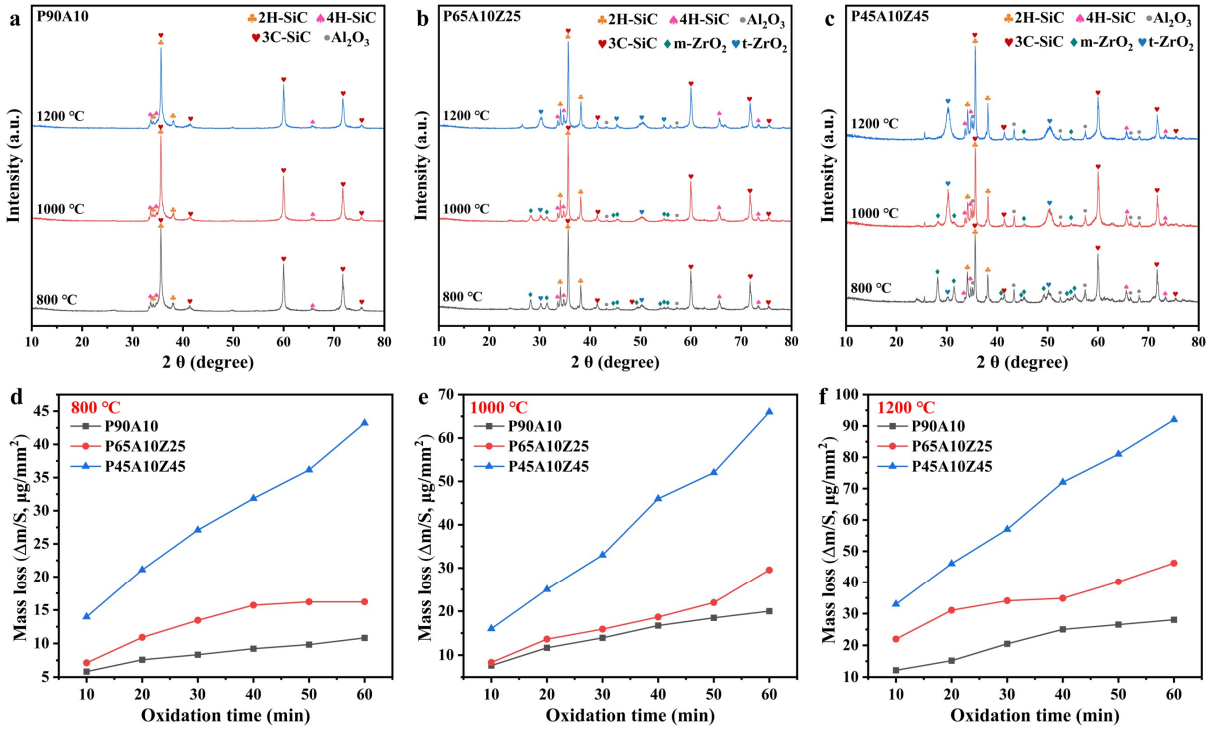

Fig. 7 Oxidation results of the samples at different temperatures

(a−c) Phase analyses of oxide layers; (d−f) Variation of unit area mass change per unit area with oxidation time

The surface morphology and oxide layer structure revealed a temperature-dependent oxidation-damage mechanism. As shown in Fig. 8 (d–i), several pores appeared on the surfaces of the oxidized samples, which were channels left by the outward escape of internally generated B_2O_3 gas. The size and number of surface pores significantly increased at higher oxidation temperatures. Cross-sectional observations of the oxide layer on P65A10Z25 further indicated that its thickness increased monotonically with temperature, measuring approximately 90, 150, and over 300 μm at 800, 1000, and 1200 ℃, respectively. In addition, the extent of internal loosening became more pronounced at higher temperatures.

The oxidation kinetics exhibited a transition from parabolic to quasi-linear behavior, allowing the effective oxidation resistance temperature window to be defined (Fig. 7). For the P65A10Z25 sample, which exhibited the optimal overall performance, the mass loss as a function of oxidation time approximately followed a parabolic law at 800 ℃ (Fig. 7(d)). This suggests that the initial oxidation process was controlled by the diffusion of oxygen ions through the gradually thickening surface oxide layer, ultimately forming a relatively stable oxide layer (about 90 μm).

When the temperature was raised to 1000 ℃ (Fig. 7(e)), the kinetics curve deviated with increasing oxidation cycles: after a brief initial stabilization period, the mass loss accelerated. This behavior corresponds to the excessive porosity and channels formed within the oxide layer owing to B_2O_3 volatilization (Fig. 7(e)). As the layer continued to thicken, its protective properties progressively declined. At 1200 ℃, the oxidation kinetics entered a quasi-linear stage characterized by oxide layer cracking and accelerated mass loss. The internal pressure generated by intense volatilization causes the formation of numerous microcracks in the oxide layer, providing direct pathways for rapid oxygen diffusion and resulting in severe degradation of the material's oxidation resistance. Notably, the characteristic fine scale and uniform distribution of precursor-derived ZrB_2 play a critical role in this process. Compared with coarser particles from powder routes, finer ZrB_2 domains offer a larger reactive surface area and shorter diffusion paths for oxidation, leading to more rapid and localized generation of B_2O_3 vapor. This inherently promotes the buildup of internal pressure and the consequent development of porosity and microcracks, ultimately compromising the protective integrity of the oxide layer.

Notably, the P45A10Z45 sample with the highest ZrB_2 content exhibited earlier oxidation resistance failure. Owing to the generation of a larger volume of B_2O_3 gas per unit time, internal volatilization pressure was higher. This caused severe blistering and spallation of the surface oxide layer (Fig. 8(h, i)) during oxidation at

1000 ℃, thereby lowering the effective upper temperature limit for oxidation resistance.

In summary, ZrB_2/(SiC-AlN) ceramic composites possess certain short-term oxidation resistance in static air within the temperature range of approximately 800–1000 ℃. Their failure is primarily governed by the volatilization of B_2O_3 (oxidation product of ZrB_2) which triggers porosity and structural damage within the oxide layer. Among the samples, P65A10Z25 with balanced composition and dense microstructure demonstrated the best oxidation performance, with an effective oxidation resistance temperature interval of about 800–1000 ℃.

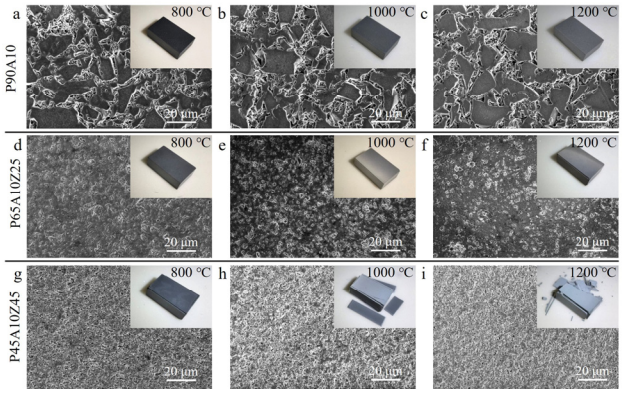

Fig. 8 Surface and macro morphologies of the samples after oxidation at different temperatures

3 Conclusions

This study demonstrates that ZrB_2 acts as an effective reinforcing phase for enhancing the mechanical properties of SiC-AlN composites. Sintering at 1950 ℃ resulted in the formation of hexagonal SiC and ZrB_2 phases, with AlN forming a solid solution within the SiC matrix. The incorporated ZrB_2 particles refined the microstructure by inhibiting SiC grain growth during high-temperature processing. This refinement led to a substantial increase in mechanical strength, with an optimal flexural strength of (407±14) MPa. Notably, the composite with 25% (in mass) ZrB_2 achieved the highest fracture toughness ((5.8±0.1) MPa·$m^{1/2}$), indicating enhanced energy dissipation and more effective stress redistribution. In contrast, the composite without ZrB_2 exhibited inferior properties, primarily due to higher porosity and reduced density. In addition to mechanical enhancement, the optimized composition exhibited stable oxidation behavior under short-term thermal exposure in air, supporting its applicability in moderately high-temperature environments. These findings confirm that *in situ* formed ZrB_2 is a potent secondary reinforcement, significantly improving the strength and toughness of SiC-AlN composites, thereby highlighting its potential for developing high-performance ceramics for demanding applications.

Supporting Materials

Supporting materials related to this article can be found at https://doi.org/10.15541/jim20260026.

References:

[1] HUANG B W, SI P Z, REN Q X, *et al*. Effect of *β* to *α* phase transformation on microstructure and thermal conductivity of SiC ceramic densified with Y_2O_3-MgO additives in argon. *Journal of the European Ceramic Society*, 2023, **43(15):** 6758.

[2] CHEN X, YIN J, HUANG L Z, *et al*. Microstructural tailoring, mechanical and thermal properties of SiC composites fabricated by selective laser sintering and reactive melt infiltration. *Journal of Advanced Ceramics*, 2023, **12(4):** 830.

[3] SHAO Q Q, GU H. Transition-layer of core–rim structures and *β*→*α* transformation in SiC ceramics. *Journal of Materiomics*, 2023, **9(2):** 299.

[4] TIAN H S, WANG L, ZHANG B H, *et al*. Fabrication of advanced bioinspired anisotropic carbide ceramic composites: past, recent progress, and future perspectives. *Journal of Advanced Ceramics*, 2024, **13(11):** 1713.

[5] ZHENG S Y, ZHANG B H, LIU X J, *et al*. *β*→*α* phase transformation and properties of solid-state-sintered SiC ceramics with TaC addition. *Materials*, 2023, **16(10):** 3878.

[6] SU B Z, LIU G L, HUANG Z R, *et al*. The effect of *in situ* synthesized AlN on densification of SiC ceramics by pressureless sintering. *Ceramics International*, 2015, **41(10):** 14172.

[7] CHEN J J, CHEN J, CHEN Z M, *et al*. Potential-current characteristics in SiC/ZrB_2 composite ceramics. *Journal of the European Ceramic Society*, 2018, **38(6):** 2477.

[8] COCK A M, SHAPIRO I P, TODD R I, *et al*. Effects of yttrium on the sintering and microstructure of alumina-silicon carbide "nanocomposites". *Journal of the American Ceramic Society*, 2005, **88(9):** 2354.

[9] YU Z J, YANG Y J, MAO K W, *et al*. Single-source-precursor synthesis and phase evolution of SiC-TaC-C ceramic nanocomposites containing core-shell structured TaC@C nanoparticles. *Journal of Advanced Ceramics*, 2020, **9(3):** 320.

[10] ZOU J, MA H B, LIU J J, *et al*. Nanoceramic composites with duplex microstructure break the strength-toughness tradeoff. *Journal of Materials Science & Technology*, 2020, **58:** 1.

[11] VALENTÍN L A, BETANCOURT J, FONSECA L F, *et al*. A comprehensive study of thermoelectric and transport properties of *β*-silicon carbide nanowires. *Journal of Applied Physics*, 2013, **114(18):** 184301.

[12] YU S W, ZENG T, ZHAO J, *et al*. Preparation and electromagnetic wave absorption properties of PDC-SiC/Si_3N_4 composites using selective laser sintering and infiltration technology. *Journal of Materials Research and Technology*, 2023, **23:** 2888.

[13] CHOWDHURY M A R, WANG K W, JIA Y J, *et al*. Electrical conductivity and structural evolution of polymer-derived SiC ceramics pyrolyzed from 1200 ℃ to 1800 ℃. *Journal of Micro and Nano-Manufacturing*, 2020, **8(2):** 024502.

[14] WANG A Q. Polymer infiltration and pyrolysis of silicon carbide ceramics using transient liquid. Pittsburgh: Doctoral Dissertation, University of Pittsburgh, 2023.

[15] BECHELANY M C, SALAMEH C, VIARD A, *et al*. Preparation of polymer-derived Si-B-C-N monoliths by spark plasma sintering technique. *Journal of the European Ceramic Society*, 2015, **35(5):**

1361.

[16] SANTHOSH B, IONESCU E, ANDREOLLI F, *et al*. Effect of pyrolysis temperature on the microstructure and thermal conductivity of polymer-derived monolithic and porous SiC ceramics. *Journal of the European Ceramic Society*, 2021, **41(2):** 1151.

[17] HE R J, DING G J, ZHANG K Q, *et al*. Fabrication of SiC ceramic architectures using stereolithography combined with precursor infiltration and pyrolysis. *Ceramics International*, 2019, **45(11):** 14006.

[18] LIU X M, YU Z J, ISHIKAWA R, *et al*. Single-source-precursor synthesis and electromagnetic properties of novel RGO-SiCN ceramic nanocomposites. *Journal of Materials Chemistry C*, 2017, **5(31):** 7950.

[19] XIA A D, ZHANG B H, YIN J, *et al*. Cross-scale microstructure design of precursor-derived SiC-AlN nanoceramic composites hybrid with *ex-situ* ZrB_2. *Advanced Powder Materials*, 2023, **2(1):** 100063.

[20] YU Z J, LI F, ZHU Q K. Single-source-precursor synthesis and phase evolution of NbC-SiC-C ceramic nanocomposites with core−shell structured NbC@C and SiC@C nanoparticles. *Advanced Powder Materials*, 2022, **1(1):** 100009.

[21] CLARK M D, WALKER L S, HADJIEV V G, *et al*. Polymer precursor-based preparation of carbon nanotube-silicon carbide nanocomposites. *Journal of the American Ceramic Society*, 2012, **95(1):** 328.

[22] ECKEL Z C, ZHOU C Y, MARTIN J H, *et al*. Additive manufacturing of polymer-derived ceramics. *Science*, 2016, **351(6268)**: 58.

[23] VIARD A, FONBLANC D, LOPEZ-FERBER D, *et al*. Polymer derived Si-B-C-N ceramics: 30 years of research. *Advanced Engineering Materials*, 2018, **20(10):** 1800360.

[24] LAADOUA H, PRADEILLES N, LUCAS R, *et al*. Preparation of ZrC/SiC composites by using polymer-derived ceramics and spark plasma sintering. *Journal of the European Ceramic Society*, 2020, **40(5):** 1811.

[25] XIA A D, YIN J, CHEN X, *et al*. Fabrication of (SiC-AlN)/ZrB_2 composite with nano-micron hybrid microstructure *via* PCS-derived ceramics route. *Materials*, 2021, **14(2):** 334.

[26] HU M G, HUANG Z L, LI X Y, *et al*. Ultrafine ZrB_2 ceramic powders prepared by a Sol-Gel method synergized with a carbothermic reaction and their improved sintering performance. *ACS Applied Engineering Materials*, 2023, **1(2):** 769.

[27] ZANGVIL A, RUH R. Phase relationships in the silicon carbide-aluminum nitride system. *Journal of the American Ceramic Society*, 1988, **71(10):** 884.

[28] HANSEN N. Hall-Petch relation and boundary strengthening. *Scripta Materialia*, 2004, **51(8):** 801.

[29] LU M Y, HAN B H, HE W H, *et al*. The strength of the ceramic matrix composites under the influence of pore is reviewed. *Journal of Physics*: *Conference Series*, 2021, **1777(1):** 012027.

[30] HE Z C, WU J J. Research on the oxidation process of micro-boron below the melting point temperature. *Acta Astronautica*, 2024, **225:** 67.

基于前驱体的 ZrB_2/(SiC-AlN)陶瓷复合材料的制备及性能研究

周 岩[1,2], 刘骐恺[2], 夏爱东[2,3], 张步豪[2,4], 殷 杰[2,3], 黄政仁[2,3]

(1. 上海大学 材料科学与工程学院, 上海 200444; 2. 中国科学院 上海硅酸盐研究所, 上海 201899; 3. 中国科学院大学 材料科学与光电技术学院, 北京 100864; 4. 诺丁汉大学 工程学院, 英国诺丁汉 NG7 2RD)

摘 要: 针对高超声速飞行器热防护系统等极端高温结构应用需求，本研究以商用聚碳硅烷与聚硼锆氧烷为前驱体，通过前驱体转化结合热压烧结工艺，在 1950 ℃成功制备了 ZrB_2/(SiC-AlN)陶瓷复合材料。X 射线衍射结果显示，烧结后产物中形成六方 SiC 相与 ZrB_2 相，未出现明显的 AlN 特征峰，证实 AlN 已固溶于 SiC 基体中，形成了 SiC-AlN 固溶体。显微结构观察结果表明，前驱体衍生的 ZrB_2 均匀分散在 SiC-AlN 基体中，不仅促进了烧结致密化，还能有效抑制基体晶粒生长。研究还系统分析了前驱体衍生 ZrB_2 含量对复合材料物相演变、显微结构特征、致密化行为以及力学性能的影响。当 ZrB_2 和 AlN 质量分数分别为 25%和 10%时，复合材料表现出最佳综合性能，其开口气孔率为 0.6%，抗弯强度达(407±14) MPa，断裂韧性为(5.8±0.1) MPa·$m^{1/2}$。同时，在 800~1000 ℃静态空气中还表现出良好的短期抗氧化性能。结果表明，基于前驱体法引入 ZrB_2 可有效调控聚合物衍生陶瓷基 SiC-AlN 复合材料的微观结构并提升其综合性能。

关 键 词: 前驱体衍生陶瓷；纳米复合材料；SiC-AlN 固溶体；韧性；强度

中图分类号: TQ174 **文献标识码:** A **文章编号:**

Supporting Materials

Fabrication of ZrB_2/(SiC-AlN) Ceramic Composites *via* SiC and ZrB_2 precursors

ZHOU Yan[1,2], LIU Qikai[2], XIA Aidong[2,3], ZHANG Buhao[2,4], YIN Jie[2,3], HUANG Zhengren[2,3]

(1. School of Materials Science and Engineering, Shanghai University, Shanghai 200444, China; 2. Shanghai Institute of Ceramics, Chinese Academy of Sciences, Shanghai 201899, China; 3. College of Materials Science and Opto-Electronic Technology, University of Chinese Academy of Sciences, Beijing 100864, China; 4. Faculty of Engineering, University of Nottingham, Nottingham NG7 2RD, UK)

Fig. S1 Thermal analysis of the ZrB_2 precursors

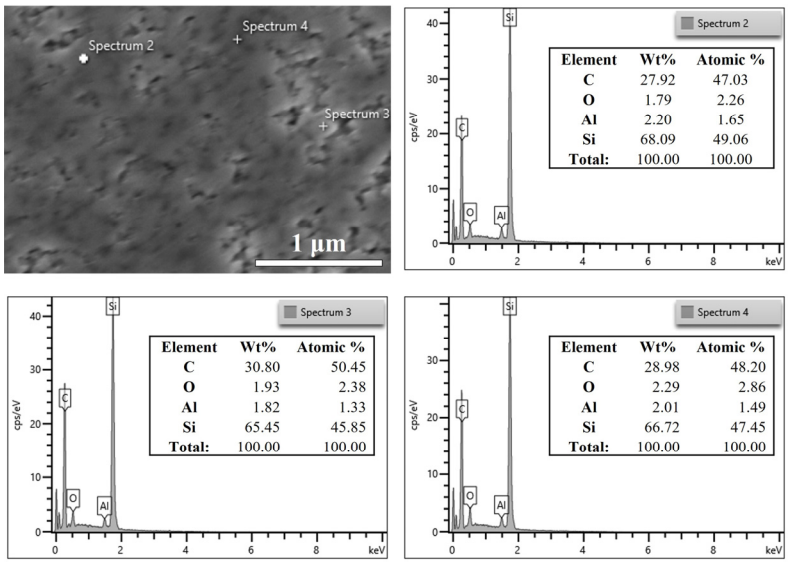

Fig. S2 The point-scan element distribution of the P90A10 sample

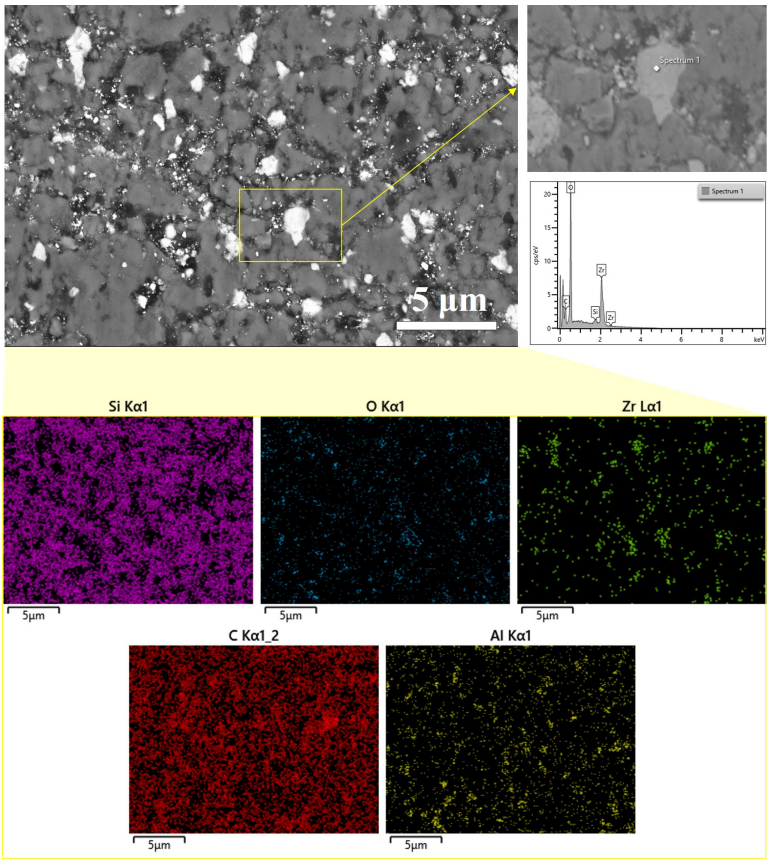

Fig. S3 The element distribution of the P65A10Z25 sample during surface scanning and point scanning